

¹ The origin of water-vapor rings in tropical cold pools

Wolfgang Langhans¹ and David M. Romps^{1,2}

Corresponding author: W. Langhans, Earth Sciences Division, Lawrence Berkeley National Laboratory, Mailstop 74R316C, Berkeley, CA 94720, USA. (wlanghans@lbl.gov)

¹Earth Sciences Division, Lawrence
Berkeley National Laboratory, Berkeley,
California, USA.

²Department of Earth and Planetary
Science, University of California, Berkeley,
California, USA.

2 Tropical deep convection over the ocean is found to grow preferentially from
3 thermodynamically pre-conditioned regions of high specific humidity and,
4 thus, high moist static energy. For this reason, rings of enhanced specific hu-
5 midity at the leading edges of evaporatively driven cold pools have recently
6 received considerable attention. The prevailing theory explains these rings
7 by the water-vapor source from the evaporation of rain drops below cloud
8 base. Their origin is studied in this letter using large-eddy simulations of in-
9 dividual cumulus clouds that rise into a tropical atmosphere over ocean. It
10 is demonstrated that – in contrast to this theory – water-vapor rings are pri-
11 marily explained by surface latent-heat fluxes rather than by the evapora-
12 tion of rain. This finding implies that conceptual models used in subgrid-scale
13 parameterizations of deep convection should consider the formation of rings
14 of increased specific humidity by the cold-pool-induced enhancement of sur-
15 face fluxes.

1. Introduction

16 The presence of cold pools within the planetary boundary layer (PBL) over tropical
17 oceans is crucial for the interaction between the PBL and the free troposphere through
18 their impact on deep convection. The modulation of deep convection by cold-pool dy-
19 namics has commonly been hypothesized to result from two processes: a) the mechanical
20 lifting of ambient air at the leading edge of cold pools as known from squall line dynamics
21 [e.g., *Moncrieff and Liu*, 1999; *Droegemeier and Wilhelmson*, 1985; *Rotunno et al.*, 1988]
22 and b) the preconditioning of the boundary layer for deep convection through cold-pool
23 induced enhancement of the moist static energy inside the PBL [*Tompkins*, 2001a, b, the
24 latter will be referred to as TO1].

25 The latter thermodynamic argument is based on the observation that cold pools exhibit
26 rings of enhanced water-vapor content and thus high moist static energy within their
27 leading edges. These rings of enhanced water-vapor content are visible from horizontal
28 distributions of near-surface water-vapor mixing ratios. They have been observed in gust
29 fronts over tropical oceans [*Addis et al.*, 1984] and have been described in various cloud-
30 resolving and large-eddy simulations of deep tropical convection and precipitating trade-
31 wind cumuli (e.g., TO1; *Xue et al.* [2008]; *Khairoutdinov et al.* [2009]; *Moeng et al.* [2009];
32 *Moeng and Arakawa* [2012]; *Seifert and Heus* [2013]; *Torri et al.* [2015]).

33 Even if convective updrafts do not originate from preconditioned air inside an active
34 cold pool (as argued by TO1), the positive moisture anomaly carried near the edges of
35 recovering cold pools will later favor the triggering upon collision with a more active (i.e.,
36 younger) cold pool. This is described in TO1, who found that convection grows from PBLs

with a pre-existing vapor anomaly of about $+1 \text{ g kg}^{-1}$. The observed vapor rings are of relevance also as they may eventually cluster to larger moist patches [Schlemmer and Hohenegger, 2014] and trigger relatively wide – thus less entraining and deeper – clouds [Boing et al., 2012]. Several other studies demonstrated that deep convective updrafts over tropical oceans preferentially grow from anomalously moist parts of the boundary layer [Kingsmill and Houze, 1999; Seifert and Heus, 2013; Li et al., 2014; Torri et al., 2015]. Understanding the mechanisms behind the formation of these vapor rings is thus critical to understanding the influence of cold pools on deep convection. Although some convection parameterizations in GCMs account for the mechanical lifting by cold pools [Qian et al., 1998; Grandpeix and Lafore, 2010; Rio et al., 2013], air is generally modeled as being lifted from the unperturbed (i.e., environmental) part of the boundary layer without accounting for the effects of these vapor rings.

Moreover, despite the agreement on the relevance of these moist anomalies, different explanations were proposed for the origin of these rings. The prevailing hypothesis proposed by TO1 is that these rings form due to the evaporation of raindrops within the sub-cloud layer before the downdraft reaches the PBL. This theory is supported by earlier observations of moistening of the subcloud layer by rain evaporation in a severe thunderstorm over the high plains [Betts, 1984]. In line with TO1, Seifert and Heus [2013] argue that evaporation of rain is key to the existence of these vapor rings. In contrast, Li et al. [2014] argue that evaporation of rain does not contribute to the anomalous moisture. To seed even more confusion, Li et al. [2014] and Schlemmer and Hohenegger [2014] conclude that, in contrast to TO1, the enhanced vapor content is found *outside* of cold pools. This

underlines the incongruity of previous explanations. On top of that, the role of surface latent-heat fluxes remains unclear.

In this paper we seek a physical explanation of the origin of these vapor rings. More specifically, we seek to answer the following questions:

1. What is the origin of water-vapor rings in tropical cold pools?
2. What are the individual contributions from evaporation of rain, surface latent-heat fluxes, and the existing (i.e., pre-rain) PBL moisture anomaly?
3. Are the underlying physics in line with the conceptual ideas proposed by TO1?

To address these questions, we carry out large-eddy simulations and study the vapor sources using passive and active tracers of water-vapor mass (see section 2). The simulations are motivated by atmospheric conditions commonly observed in radiative-convective equilibrium (RCE) over tropical oceans.

2. Numerical setup

2.1. General description

Numerical simulations are carried out using Das Atmosphärische Modell [DAM, *Romps*, 2008]. DAM solves the compressible equations in flux form using a split-explicit [*Klemp et al.*, 2007] total-variation-diminishing (TVD) 3rd-order Runge-Kutta (RK3) discretization in time [*Shu and Osher*, 1988]. Advection is discretized using a 3rd-order upstream scheme and a positive-definite flux limiter [*Thuburn*, 1996] is applied to the moisture scalars. Following the concept of implicit LES [e.g., *Margolin et al.*, 2006], no subgrid-scale (SGS) turbulence closure is applied. The lateral boundary conditions are periodic.

78 A no-slip bottom boundary condition is applied and surface drag and sensible and
 79 latent-heat fluxes are parameterized by bulk transfer laws using a drag coefficient of
 80 $C_d = 1.5 \times 10^{-3}$. If not mentioned otherwise, the surface moisture flux is parameterized
 81 as $\rho \overline{q'_v w'}|_s = -C_e |\mathbf{u}|_1 (q_v|_1 - q_v^*|_{\text{sst}})$ with $C_e = C_d$, with $q_v^*|_{\text{sst}}$ the saturation specific humidity
 82 for a sea surface temperature (SST) of 300 K, and with index 1 denoting variables on the
 83 first model level.

84 The microphysical mass exchange rates among six water classes are parameterized using
 85 the Lin-Lord-Krueger one-moment bulk scheme [Lin *et al.*, 1983; Lord *et al.*, 1984; Krueger
 86 *et al.*, 1995] with minor adaptions as described by Langhans *et al.* [2015]. The bulk
 87 formulation distinguishes between six water classes: water vapor, cloud liquid water,
 88 cloud ice, rain, snow, and graupel.

2.2. Simulations

89 Single cumulus clouds are simulated in this study similar to the ones investigated by
 90 Langhans *et al.* [2015]. Clouds are forced from an initially axisymmetric “bubble” pertur-
 91 bation in the center of the numerical domain. The advantage of this configuration is that
 92 the emerging cold pool remains quasi-axisymmetric without any collisions with other cold
 93 pools as it would be in simulations of RCE. Motivated by cold pools commonly observed
 94 in RCE, the initialized background temperature and specific humidity profiles $T_0(z)$ and
 95 $q_{v0}(z)$ are taken from previously conducted RCE runs over an SST of 300 K [see Romps
 96 and Kuang, 2011, section 3].

97 We focus on simulating the period of cold-pool initiation and propagation. The domain
 98 and grid setup are thus tailored to achieve high resolution inside the boundary layer with

a relatively coarse and inexpensive resolution above. The dimensions of the numerical domain are $(L_x, L_y, L_z) = (20, 20, 14.1)$ km. A five-layer structure is used to distribute levels in the vertical. Three sections with constant grid spacings δz of 10, 190, and 610 m, respectively, are separated by two sections that allow for smooth transitions based on tanh functions. The interfaces between the layers are located at 400, 3400, 5300, and 9300 m. The lowermost layer with $\delta z = 10$ m fully includes the emerging cold pools. The horizontal grid spacing is 50 m. The RK3 dynamics are solved using an adaptive time stepping to satisfy a maximum local CFL of 0.5.

A reference simulation, R1, and a sensitivity experiment R2 are presented in this letter. Moist convection in R1 is initiated from an anomalously warm and moist boundary layer that exhibits a Gaussian-distributed perturbation of $q'_{v0} = 1 \text{ g kg}^{-1}$ with a half width of 3 km. This moisture anomaly is thought to represent the moisture excess caused by an older cold pool and the chosen scale and magnitude is in line with findings in TO1 (his Fig. 7) and others (see introduction). The sensitivity to this initialized moisture perturbation is tested in run R2 which starts without this moisture perturbation.

To kick off convection, a small-scale temperature perturbation of magnitude $\delta T = 1 \text{ K}$ is prescribed in both R1 and R2, as

$$T(r, z) = T_0(z) + (\delta T + \zeta) \exp \left[-(r/r_b)^2 - (z/z_b)^2 \right], \quad (1)$$

with $r = \sqrt{x^2 + y^2}$, height z , $r_b = 1000 \text{ m}$, $z_b = 500 \text{ m}$, and random perturbations $\zeta \in [-0.05, 0.05]$. In case of R1, the q_v perturbation is added as

$$q_v(r, z) = q_{v0}(z) + q'_{v0} \exp \left[-(r/R_b)^2 - (z/Z_b)^2 \right], \quad (2)$$

₁₁₄ with $q'_{v0} = 10^{-3}$ g g⁻¹, $R_b = 3000$ m, and $Z_b = 500$ m. Simulations are carried out for
₁₁₅ two hours to capture the full life cycle of the cloud, including the dissipating stage and –
₁₁₆ most importantly – cold-pool propagation.

₁₁₇ Three further experiments were carried out to test the sensitivity to the surface transfer
₁₁₈ coefficient C_e . These are described in the supporting information (text S1 and Fig. S2).
₁₁₉ One of them applies Monin-Obukhov similarity theory [Dyer and Hicks, 1970; Stull, 1988])
₁₂₀ to compute the surface latent-heat flux. This experiment results in even larger surface
₁₂₁ latent-heat fluxes than obtained by reference run R1.

2.3. Water-vapor tracers

₁₂₂ The individual contributions to the ring-shaped water-vapor mass anomaly are identified
₁₂₃ here by advancing tracers of water-vapor mass of different origin. To do so, tracer mass
₁₂₄ fractions are initialized at time $t_i = 1040$ s, which is right before rain starts falling into
₁₂₅ the sub-cloud layer (i.e., pre-rain). A first (passive) tracer mass fraction q'_{pbl} represents
₁₂₆ the pre-rain PBL perturbation existing at time t_i . To define this perturbation, the water-
₁₂₇ vapor field at time t_i is decomposed into a base state q_{base} and a perturbation q'_{pbl} . The
₁₂₈ former is horizontally uniform inside the sub-cloud layer and defined as

$$q_{\text{base}}(x, y, z, t_i) = \gamma(z) q_v(x, y, z, t_i) + [1 - \gamma(z)] q_v^\infty(z) \quad (3)$$

$$\gamma(z) = 0.5 + 0.5 \tanh[0.02(z - 500)], \quad (4)$$

₁₂₉ with $q_v^\infty(z) = q_v(-L_x/2, -L_y/2, z, t_i)$ the specific humidity profile in a corner of the do-
₁₃₀ main. The perturbation q'_{pbl} is defined as $q'_{\text{pbl}} = q_v - q_{\text{base}}$. Function $\gamma(z)$ goes from 0 to
₁₃₁ 1 across the cloud base at 500 m, such that q_{base} is horizontally uniform below cloud base

₁₃₂ and $q_{\text{base}} = q_v$ and $q'_{\text{pbl}} = 0$ above cloud base at time t_i . The base-state mass fraction
₁₃₃ q_{base} forms the second passive tracer to be advanced. Moreover, two active tracer mass
₁₃₄ fractions q'_{lh} and q'_{er} are advanced to study the water-vapor mass due to surface latent-heat
₁₃₅ fluxes and due to evaporation of rain, respectively. Both are initialized to zero at time t_i .

The mass M_χ of each tracer χ is advanced as

$$\frac{\partial(q_\chi\rho)}{\partial t} = -\frac{\partial(q_\chi\rho\mathbf{u})}{\partial\mathbf{x}} + S_\chi, \quad (5)$$

₁₃₆ with tracer mass fraction $q_\chi = M_\chi/(M_a + M_v + M_l + M_s)$, density ρ , mass of dry air M_a ,
₁₃₇ water vapor M_v , liquid water M_l , and solid water M_s , and tracer mass source S_χ . The
₁₃₈ source term is zero for the two passive tracers q_{base} and q'_{pbl} . The sources of the active
₁₃₉ tracers q'_{lh} and q'_{er} are the surface moisture flux convergence $S_{\text{lh}} = -\partial_z\rho\overline{q'_v w'}|_s$ and the
₁₄₀ evaporation of rain $S_{\text{er}} = \rho E$, respectively.

₁₄₁ We find that, at any time, the sum of q_{base} , q'_{pbl} , q'_{lh} , and q'_{er} is almost identical to q_v . The
₁₄₂ difference is significantly smaller than the water-vapor perturbations we are interested in,
₁₄₃ confirming that surface latent-heat fluxes and evaporation of rain are the only sources of
₁₄₄ relevance to the water-vapor budget of cold pools in our simulations.

3. The origin of water-vapor rings

3.1. Horizontal distributions

Our simulations reveal considerable agreement with both previous observational and modeling studies of cold pools formed by tropical convection (e.g., *Young et al. [1995]*; *TO1*; *Moeng et al. [2009]*; *Zuidema et al. [2012]*; *Torri et al. [2015]*; *Feng et al. [2015]*). The cold pool simulated by R1 reaches a radius of about 7 km at the end of the simulation. In agreement with modeled cold pools in *Feng et al. [2015]* (see their Fig. 6), average

propagation speeds of the leading edge are about 1.5 m s^{-1} , the potential temperature depression in the center reaches from about -1.4 K initially to 0.0 K in the recovering stage, and the lifetime is about 1.5 hours. The evolution of the radial velocity and the potential temperature are illustrated in Fig. S1 of the supporting information. In particular agreement with previous modeling studies, distinct water-vapor rings appear near the edge of radially spreading cold pools with specific humidities about 0.6 to 1.0 g kg^{-1} higher than in the unperturbed PBL away from the cold pool. To illustrate this and to identify the origin of these rings, we show density-weighted vapor mass fractions for the lowest 100 meters, defined as

$$\bar{q}'_v = \frac{\int_0^{100\text{m}} dz' \rho(z') q'_v(z')}{\int_0^{100\text{m}} dz' \rho(z')}, \quad (6)$$

¹⁴⁵ with $q'_v(x, y, z) = q_v(x, y, z) - q_v^\infty(z)$ a perturbation with respect to the far-field environment at time t_i . Analogously, average mass fractions are computed for the base-state ¹⁴⁶ perturbation $q'_{\text{base}} = q_{\text{base}} - q_v^\infty$, for the pre-rain PBL perturbation q'_{pbl} , for the latent-heat ¹⁴⁷ flux perturbation q'_{lh} , and for the perturbation q'_{er} due to evaporation. The evolution of ¹⁴⁸ these average mass fractions is illustrated for R1 in Fig. 1 by showing snapshots after ¹⁴⁹ 26, 62, and 98 minutes. To very good approximation, the actual perturbation of the ¹⁵⁰ vapor mass fraction shown in the first column results from the sum of the individual ¹⁵¹ vapor mass fraction shown in the other columns.

¹⁵² During the early stage, at $t = 26 \text{ min}$, the water-vapor ring consists mostly of water-¹⁵³ vapor mass that existed already in the PBL before the onset of rainfall. The pre-rain ¹⁵⁴ PBL water-vapor mass gets displaced laterally by the approaching dry air from aloft. At ¹⁵⁵ that time, the contributions from latent-heat fluxes and from evaporation of rain are very ¹⁵⁶

₁₅₇ small ($\leq 0.2 \text{ g kg}^{-1}$) inside regions with anomalously high vapor contents. The water-
₁₅₈ vapor mass originating from rain peaks inside the cold pool and is collocated with the
₁₅₉ negative perturbation due to the downward advection of the base state.

₁₆₀ The vapor perturbation from surface fluxes grows rapidly in time and, by $t = 62 \text{ min}$,
₁₆₁ has reached peak magnitudes larger than those due to the pre-rain PBL anomaly. Then,
₁₆₂ only the water-vapor mass from surface fluxes causes a distinct narrow ring-like anomaly.
₁₆₃ The largest mass fractions from evaporated rain are carried in the dry air mass that sunk
₁₆₄ down from aloft. The water-vapor mass from evaporation thus peaks in the dry center
₁₆₅ of the cold pool with a relatively homogeneous mass distribution towards the outer edge.
₁₆₆ The pre-rain PBL perturbation gets dispersed radially outwards in time leading to an
₁₆₇ increasing areal coverage and to decreasing peak perturbations.

3.2. Vertical distributions

₁₆₈ To better understand the transport and origin of water-vapor mass inside the cold pool,
₁₆₉ we analyze the average vertical distribution of water-vapor density and its individual
₁₇₀ contributions in a next step. We first identify the radius at the leading edge of the cold-
₁₇₁ pool $R(\varphi)$ for each azimuth angle φ . This gives a normalized radius $r^* = r/R$ for each
₁₇₂ grid column. Averaging is then applied over grid points that fall into the same r^* bins.
₁₇₃ This way, we avoid the blurring that would result from azimuthal averaging over r bins.
₁₇₄ At a given time, $R(\varphi)$ is here identified based on a filtered version of the kinetic energy
₁₇₅ field $E_w(\varphi, r) = 0.5w(\varphi, r)^2$ at $z = 15 \text{ m}$. $R(\varphi)$ is taken as the maximum radius at which
₁₇₆ $E_w(\varphi, r)$ exceeds a threshold value. This method takes advantage of the lifting that occurs
₁₇₇ right in front of the cold pool and $r^* = 1$ thus lies slightly ahead of the cold-pool edge.

¹⁷⁸ Figure 2 shows the obtained r^* -z distributions of water-vapor density ($\rho_v = q_v \rho$; gray
¹⁷⁹ shading) for the same three time steps after 26, 62, and 98 min. Also shown are contours of
¹⁸⁰ the three tracer mass density distributions due to latent-heat fluxes ($\rho'_{lh} = q'_{lh} \rho$; orange),
¹⁸¹ evaporation of rain ($\rho'_{er} = q'_{er} \rho$; blue), and the pre-rain PBL water-vapor perturbation
¹⁸² ($\rho'_{pbl} = q'_{pbl} \rho$; red). These are contoured every 0.2 kg^{-1} (line labels are multiplied by 10).
¹⁸³ The average R is indicated on top of each panel.

¹⁸⁴ During the early stage, at $t = 26$ min, the downdraft air undercuts the boundary-layer
¹⁸⁵ air mass. The displaced air indeed carries the largest moisture content, but not – as pre-
¹⁸⁶ viously argued by TO1 and others – due to evaporative moistening, but because the PBL
¹⁸⁷ was relatively moist in the first place. The water-vapor mass from evaporation that is car-
¹⁸⁸ ried by air between the leading edge and the center ($\sim 0.2 \text{ g kg}^{-1}$) is considerably smaller
¹⁸⁹ than the pre-rain water-vapor perturbation carried in the leading edge ($\sim 1.2 \text{ g kg}^{-1}$).
¹⁹⁰ The contribution from surface fluxes is also small at that time. It peaks near the surface
¹⁹¹ close to the leading edge.

¹⁹² Later, after 62 and 98 minutes, the perturbation is mostly made up by water-vapor mass
¹⁹³ that was supplied by surface latent-heat fluxes. The latter cause a distinct perturbation
¹⁹⁴ near the leading edge with considerable vertical extent. In line with laboratory flows of
¹⁹⁵ density currents [e.g., *Simpson and Britter, 1979*], the near-surface flow inside the cold
¹⁹⁶ pool is considerably faster (about twice; see Fig. S1) than the propagation speed of the
¹⁹⁷ leading edge. This leads to the enhancement of surface fluxes as seen previously from
¹⁹⁸ observations [*Johnson and Nicholls, 1983; Addis et al., 1984; Young et al., 1995; Zuidema*
¹⁹⁹ *et al., 2012; Yokoi et al., 2014; Feng et al., 2015*] and modeling studies (e.g., TO1; *Re-*

²⁰⁰ *delsperger et al. [2000]; Moeng et al. [2009]; Feng et al. [2015])* and to the transport towards
²⁰¹ and into the leading edge of the cold pool. At $t = 98$ min, the pre-rain PBL moisture has
²⁰² been lofted off the ground and significantly dispersed with minor contributions near the
²⁰³ leading edge. The bulk of the evaporated rain mass trails behind the leading edge of the
²⁰⁴ cold pool with small contributions to the low-level perturbation near $r^* = 1$. Note also
²⁰⁵ that the vapor mass perturbation is clearly carried inside the cold pool and not outside
²⁰⁶ or ahead of the leading edge as argued by *Schlemmer and Hohenegger [2014]* and *Li et al.*
²⁰⁷ [2014].

4. PBL pre-moistening by evaporating rain?

²⁰⁸ Apparently, the evaporation of rain explains only a small fraction of the water-vapor
²⁰⁹ perturbation near the leading edge of cold pools. This is in sharp contrast to the prevailing
²¹⁰ theory developed by TO1 which implies that the boundary-layer air gets moistened by the
²¹¹ evaporation of rain drops. A necessary condition for the validity of this theory is that there
²¹² is sufficient evaporation of rain drops before the original sub-cloud layer air gets replaced
²¹³ by dry downdraft air from aloft. In other words, the time t_{req} required to moisten the
²¹⁴ sub-cloud layer by about 0.7 g kg^{-1} (the magnitude of the vapor-ring anomaly; see Fig. 1)
²¹⁵ has to be equal or smaller than the time t_{exp} during which the original sub-cloud layer air
²¹⁶ is exposed to rain drops. The sub-cloud layer will get squashed outside of the rain shaft
²¹⁷ by the approaching downdraft air. The latter thus sets t_{exp} .

It is demonstrated here that the ratio $t_{\text{req}}/t_{\text{exp}}$ is around three, even if an upper bound
on t_{exp} is considered. An upper bound on t_{exp} is obtained as the time it takes an air
parcel to sink from cloud base to the ground if it experiences only the minimal negative

buoyancy due to the weight of condensate. Additional factors – which decrease t_{exp} – such as the additional acceleration due to evaporation of liquid water or an existing downdraft at cloud base are neglected. Starting from a zero velocity at cloud base, the downdraft velocity (defined to be negative downward) is assumed to evolve according to the plume model of *Simpson and Wiggert* [1969], which has been applied previously to updrafts [*Jakob and Siebesma*, 2003; *Siebesma et al.*, 2003; *Gregory*, 2001] and downdrafts *Park* [2014], as

$$\frac{dw}{dt} = 0.5 \frac{dw^2}{dz} = aB + b\epsilon w^2. \quad (7)$$

In line with our desire to obtain an upper bound on t_{exp} , this model accounts for the adverse pressure gradient due to the arising inertial pressure and considers the drag due to lateral mixing. Following *Gregory* [2001] and *Jakob and Siebesma* [2003], we use $a = 1/3$ and $b = 2$. A constant negative buoyancy B is assumed that results only from condensate loading in the rain shaft below cloud base, such that $B = -gr_l/(1 + r_t)$ with g the gravitational acceleration, r_l the rain mixing ratio, and $r_t = r_v + r_l$ the total water mixing ratio. The analytical solution for $w(z)$ is given in the appendix. Given $w(z)$, the time t_{exp} it takes to sink from $z = h$ to $z = 0$ is obtained by integrating $dt = w(z)^{-1} dz$, which gives

$$t_{\text{exp}} = \frac{1}{\sqrt{-B}\sqrt{ab\epsilon}} \tanh^{-1} \left(\sqrt{1 - e^{-2beh}} \right). \quad (8)$$

²¹⁸ For a cloud base at $h = 500$ m and a typical value of the fractional entrainment rate
²¹⁹ $\epsilon = 0.5 \cdot 10^{-3}$ m⁻¹, one yields exposure times $t_{\text{exp}} = [350, 303, 271]$ s for the simulated
²²⁰ range in rain mixing ratios of $r_l = [3, 4, 5]$ g kg⁻¹.

²²¹ The required time t_{req} is given as $t_{\text{req}} = \delta r_v / \bar{E}$ with δr_v the simulated vapor-ring per-
²²² turbation of 0.7 g kg⁻¹ (see Fig. 1) and \bar{E} an average evaporation rate in the sub-cloud

²²³ layer. The latter is $0.8 \cdot 10^{-6} \text{ s}^{-1}$ in R1, yielding $t_{\text{req}} = 875 \text{ s}$. Thus, $t_{\text{req}}/t_{\text{exp}}$ ranges
²²⁴ between 2.5 and 3.2 for the specified range of rain mixing ratios. This simple estimate
²²⁵ shows that – at best – only about one third of the anticipated δr_v can result from the
²²⁶ evaporation of rain below cloud base. These numbers agree fairly well with our reference
²²⁷ simulation which showed an evaporative water-vapor source of about 0.2 g kg^{-1} before
²²⁸ air gets displaced laterally by the downdraft. Note also that a sensitivity experiment in
²²⁹ which the evaporation of rain had been switched off resulted in the same dynamics in
²³⁰ the sub-cloud layer during this initial stage of rainfall onset. Thus, the acceleration that
²³¹ squashes the sub-cloud air aside is indeed maintained by condensate loading rather than
²³² by the evaporation of rain drops.

5. Sensitivity to initial PBL moisture

²³³ The evaporation rate E of rain drops in the sub-cloud layer is largely controlled by
²³⁴ relative humidity. Then, what if moist convection forms from a drier sub-cloud layer?
²³⁵ Will the source from rain-drop evaporation increase due to larger evaporation rates?
²³⁶ To test this, we analyze simulation R2 and again decompose the water-vapor pertur-
²³⁷ bation in the lowest 100 m into its different origins. The results are shown for two time
²³⁸ steps (26 and 98 min) in Fig. 3. Even though this simulation is initialized without a PBL
²³⁹ moisture anomaly, surface latent-heat fluxes during the convergent period of convective
²⁴⁰ growth form a pre-rain moisture anomaly below the cloud. The surface-flux contribution
²⁴¹ to the pre-rain anomaly is even larger than in R1, simply because R2 is drier than R1 and
²⁴² the surface latent-heat fluxes scale with the moisture gradient at the surface (see section
²⁴³ 2.1). For this reason, the pre-rain sub-cloud layer in R2 is not as dry as would be expected

in the absence of this feedback. On top of that, rain mixing ratios r_l in the rain shaft are smaller than in R1 (not shown). This weakening of convective precipitation for a drier initial boundary layer is in line with findings presented by *Droegemeier and Wilhelmson* [1985] (their section 5b). Overall, the increase of E due to a smaller r_v is even overcompensated by the decrease due to smaller r_l . The ratio of $t_{\text{req}}/t_{\text{exp}}$ in R2 remains close to the one in R1 as both t_{req} and t_{exp} increase. As a result, the evaporative contribution to the water-vapor perturbation is again insignificant in R2 (see Fig. 3). As in R1, surface latent-heat fluxes are the key player.

6. Conclusions

Rings of enhanced water-vapor concentrations are associated with the leading edges of cold pools over tropical oceans. The idealized simulations of single cold pools carried out in this letter replicate this observation for an atmosphere initialized with thermodynamic profiles from radiative-convective equilibrium. In contrast to the prevailing theory, the findings presented herein show that surface latent-heat fluxes are the primary cause for such ring-shaped water-vapor anomalies. The evaporation of rain drops below cloud base is found to be secondary since the sub-cloud layer is not exposed long enough to the rain shaft before it gets displaced by the approaching dry downdraft air. The sub-cloud air which gets displaced by the downdraft is indeed relatively moist, but not – as previously believed – due to rain-drop evaporation, but simply because deep convection grows from a relatively moist sub-cloud layer in the first place. Figure 4 summarizes the processes relevant during different stages of the cold pool’s life cycle.

264 To advance the parameterization of cold-pool effects on deep convection in GCMs, it
 265 thus appears key to represent the effects of surface latent-heat fluxes within conceptual
 266 models for subgrid-scale convection. Based on our results, a parameterization should
 267 account for the enhanced latent-heat fluxes into the cold pool and the subsequent mass
 268 transport into the cold-pool edges. Future research needs to establish a conceptual model
 269 for the evolution of the magnitude of these water-vapor rings. On top of that, the effects
 270 of enhanced water-vapor content on, e.g., convective inhibition, need to be considered to
 271 account for the modified lifting trajectories of such thermodynamically conditioned air
 272 parcels.

Appendix A: Analytical solution for $w(z)$

For constant b , ϵ , a , and B the analytical solution to (7) is

$$w(z) = -\sqrt{w(h)^2 e^{-2b\epsilon(h-z)} - \frac{aB}{b\epsilon} [1 - e^{-2b\epsilon(h-z)}]}, \quad (\text{A1})$$

273 with $0 \leq z \leq h$, h the height at cloud base, and $B \leq 0$.

274 **Acknowledgments.** This work was supported by the U.S. Department of Energy's
 275 Atmospheric System Research, an Office of Science, Office of Biological and Environ-
 276 mental Research program, and by the Scientific Discovery through Advanced Computing
 277 (SciDAC) program funded by U.S. Department of Energy Office of Advanced Scientific
 278 Computing Research and Office of Biological and Environmental Research, under Con-
 279 tract No. DE-AC02-05CH11231. This research used computing resources of the National
 280 Energy Research Scientific Computing Center (NERSC), which is supported by the Of-
 281 fice of Science of the U.S. Department of Energy under Contract DE-AC02-05CH11231,

and computing resources of the Extreme Science and Engineering Discovery Environment (XSEDE), which is supported by National Science Foundation Grant OCI-1053575. W.L. likes to thank N. Jeevanjee for helpful discussions. Profiles used to initialize DAM are available from the corresponding author.

References

- Addis, R. P., M. Garstang, and G. D. Emmitt (1984), Downdrafts from tropical oceanic cumuli, *Bound.-Layer Meteorol.*, *28*, 23–49.
- Betts, A. K. (1984), Boundary layer thermodynamics of a high plains severe storm, *Mon. Wea. Rev.*, *112*, 2199–2211.
- Boing, S. J., H. J. J. Jonker, A. P. Siebesma, and W. W. Grabowski (2012), Influence of the Subcloud Layer on the Development of a Deep Convective Ensemble, *J. Atmos. Sci.*, *69*, 2682–2698.
- Droegemeier, K. K., and R. B. Wilhelmson (1985), Three-dimensional numerical modeling of convection produced by interacting thunderstorm outflows. part I: Control simulation and low-level moisture variations, *J. Atmos. Sci.*, *42*, 2381–2403.
- Dyer, A. J., and B. B. Hicks (1970), Flux-gradient relationships in the constant flux layer, *Quart. J. Roy. Meteor. Soc.*, *96*, 715–721.
- Feng, Z., S. Hagos, A. K. Rowe, C. D. Burleyson, M. N. Martini, and S. P. de Szoeke (2015), Mechanisms of convective cloud organization by cold pools over tropical warm ocean during the AMIE/DYNAMO field campaign, *J. Adv. Model. Earth Syst.*, *7*, 1–25.
- Grandpeix, J.-Y., and J.-P. Lafore (2010), A density current parameterization coupled with emanuels convection scheme. Part I: The models, *J. Atmos. Sci.*, *67*, 881–897.

- 303 Gregory, D. (2001), Estimation of entrainment rate in simple models of convective clouds,
304 *Quart. J. Roy. Meteor. Soc.*, 127, 53–72.
- 305 Jakob, C., and A. P. Siebesma (2003), A new subcloud model for mass-flux convection
306 schemes: Influence on triggering, updraft properties, and model climate, *Mon. Wea.
307 Rev.*, 131, 2765–2778.
- 308 Johnson, R. H., and M. E. Nicholls (1983), A composite analysis of the boundary-layer
309 accompanying a tropical squall line, *Mon. Wea. Rev.*, 111, 308–319.
- 310 Khairoutdinov, M. F., S. K. Krueger, C.-H. Moeng, P. A. Bogenschutz, and D. A. Randall
311 (2009), Large-eddy simulation of maritime deep tropical convection, *J. Adv. Model.
312 Earth Syst.*, 1, 13, doi:10.3894/JAMES.2009.1.15.
- 313 Kingsmill, D. E., and R. A. Houze (1999), Thermodynamic characteristics of air flowing
314 into and out of precipitating convection over the west pacific warm pool, *Quart. J. Roy.
315 Meteor. Soc.*, 125, 1209–1229.
- 316 Klemp, J. B., W. C. Skamarock, and J. Dudhia (2007), Conservative split-explicit time
317 integration methods for the compressible nonhydrostatic equations, *Mon. Wea. Rev.*,
318 135, 2897–2913.
- 319 Krueger, S. K., Q. A. Fu, K. N. Liou, and H. N. S. Chin (1995), Improvements of an
320 ice-phase microphysics parameterization for use in numerical simulations of tropical
321 convection, *J. Appl. Meteorol.*, 34, 281–287.
- 322 Langhans, W., K. Yeo, and D. M. Romps (2015), Lagrangian investigation of the precip-
323 itation efficiency of convective clouds, *J. Atmos. Sci.*, 72, 1045–1062.

- ³²⁴ Li, Z., P. Zuidema, and P. Zhu (2014), Simulated convective invigoration processes at
³²⁵ trade wind cumulus cold pool boundaries, *J. Atmos. Sci.*, *71*, 2823–2841; Corrigendum,
³²⁶ *71*, 4710.
- ³²⁷ Lin, Y.-L., D. F. Richard, and H. D. Orville (1983), Bulk parametrization of the snow
³²⁸ field in a cloud model, *J. Appl. Meteor.*, *22*, 1065–1092.
- ³²⁹ Lord, S. J., H. E. Willoughby, and J. M. Piotrowicz (1984), Role of a parameterized
³³⁰ ice-phase microphysics in an axisymmetric, nonhydrostatic tropical cyclone model, *J.*
³³¹ *Atmos. Sci.*, *41*, 2836–2848.
- ³³² Margolin, L. G., W. J. Rider, and F. F. Grinstein (2006), Modeling turbulent flow with
³³³ implicit LES, *J. Turbul.*, *7*, 1–27.
- ³³⁴ Moeng, C.-H., and A. Arakawa (2012), Representation of boundary layer moisture trans-
³³⁵ port in cloud-resolving models, *Mon. Wea. Rev.*, *140*, 3682–3698.
- ³³⁶ Moeng, C.-H., M. A. LeMone, M. F. Khairoutdinov, S. K. Krueger, P. A. Bogenschutz,
³³⁷ and D. A. Randall (2009), The tropical marine boundary layer under a deep convec-
³³⁸ tion system: a large-eddy simulation study, *J. Adv. Model. Earth Syst.*, *1*, 13, doi:
³³⁹ 10.3894/JAMES.2009.1.15.
- ³⁴⁰ Moncrieff, M. W., and C. Liu (1999), Convection initiation by density currents: Role of
³⁴¹ convergence, shear, and dynamical organization, *Mon. Wea. Rev.*, *127*, 2455–2464.
- ³⁴² Park, S. (2014), A Unified Convection Scheme (UNICON). Part I: Formulation, *J. Atmos.*
³⁴³ *Sci.*, *71*, 3902–3930.
- ³⁴⁴ Qian, L., G. S. Young, and W. M. Frank (1998), A convective wake parameterization
³⁴⁵ scheme for use in general circulation models, *Mon. Wea. Rev.*, *126*, 456–469.

- ³⁴⁶ Redelsperger, J., F. Guichard, and S. Mondon (2000), A parameterization of mesoscale
³⁴⁷ enhancement of surface fluxes for large-scale models, *J. Climate*, *13*, 402–421.
- ³⁴⁸ Rio, C., et al. (2013), Control of deep convection by sub-cloud lifting processes: the ALP
³⁴⁹ closure in the LMDZ5B general circulation model, *Clim. Dyn.*, *40*, 2271–2292.
- ³⁵⁰ Romps, D. M. (2008), The Dry-Entropy Budget of a Moist Atmosphere, *J. Atmos. Sci.*,
³⁵¹ *65*, 3779–3799.
- ³⁵² Romps, D. M., and Z. Kuang (2011), A Transient Matrix for Moist Convection, *J. Atmos.*
³⁵³ *Sci.*, *68*, 2009–2025.
- ³⁵⁴ Rotunno, R., J. B. Klemp, and M. L. Weisman (1988), A theory for strong, long-lived
³⁵⁵ squall lines, *J. Atmos. Sci.*, *45*, 463–485.
- ³⁵⁶ Schlemmer, L., and C. Hohenegger (2014), The formation of wider and deeper clouds as
³⁵⁷ a result of cold-pool dynamics, *J. Atmos. Sci.*, *71*, 2842–2858.
- ³⁵⁸ Seifert, A., and T. Heus (2013), Large-eddy simulation of organized precipitating trade
³⁵⁹ wind cumulus clouds, *Atmos. Chem. Phys.*, *13*, 5631–5645.
- ³⁶⁰ Shu, C. W., and S. Osher (1988), Efficient implementation of essentially non-oscillatory
³⁶¹ shock-capturing schemes, *J. Comput. Phys.*, *77*, 439–471.
- ³⁶² Siebesma, A. P., C. S. Bretherton, A. Brown, et al. (2003), A large eddy simulation
³⁶³ intercomparison study of shallow cumulus convection, *J. Atmos. Sci.*, *60*, 1201–1219.
- ³⁶⁴ Simpson, J., and V. Wiggert (1969), Models of precipitating cumulus towers, *Mon. Wea.*
³⁶⁵ *Rev.*, *97*, 471–489.
- ³⁶⁶ Simpson, J. E., and R. E. Britter (1979), The dynamics of the head of a gravity current
³⁶⁷ advancing over a horizontal surface, *J. Fluid Mech.*, *94*, 477–495.

- ³⁶⁸ Stull, R. B. (1988), *An introduction to boundary layer meteorology*, 666 pp., Kluwer Academic Publishers.
- ³⁶⁹
- ³⁷⁰ Thuburn, J. (1996), Multidimensional flux-limited advection schemes, *J. Comput. Phys.*, 123, 74–83.
- ³⁷¹
- ³⁷² Tompkins, A. M. (2001a), Organization of tropical convection in low vertical wind shears: The role of water vapor, *J. Atmos. Sci.*, 58, 529–545.
- ³⁷³
- ³⁷⁴ Tompkins, A. M. (2001b), Organization of tropical convection in low vertical wind shears: The role of cold pools, *J. Atmos. Sci.*, 58, 1650–1672.
- ³⁷⁵
- ³⁷⁶ Torri, J., Z. Kuang, and Y. Tian (2015), Mechanisms for convection triggering by cold pools, *Geophys. Res. Lett.*, 42, 1943–1950.
- ³⁷⁷
- ³⁷⁸ Xue, H., G. Feingold, and B. Stevens (2008), Aerosol effects on clouds, precipitation, and the organization of shallow cumulus convection, *J. Atmos. Sci.*, 65, 392–406.
- ³⁷⁹
- ³⁸⁰ Yokoi, S., M. Katsumata, and K. Yoneyama (2014), Variability in surface meteorology and air-sea fluxes due to cumulus convective systems observed during CINDY/DYNAMO, *J. Geophys. Res.*, 119, 2064–2078.
- ³⁸¹
- ³⁸² Young, G. S., S. M. Perugini, and C. W. Fairall (1995), Convective wakes in the equatorial western Pacific during TOGA, *Mon. Wea. Rev.*, 123, 110–123.
- ³⁸³
- ³⁸⁴ Zuidema, P., Z. Li, R. J. Hill, L. Bariteau, B. Rilling, C. Fairall, W. A. Brewer, B. Albrecht, and J. Hare (2012), On Trade Wind Cumulus Cold Pools, *J. Atmos. Sci.*, 69, 258–280.
- ³⁸⁵
- ³⁸⁶

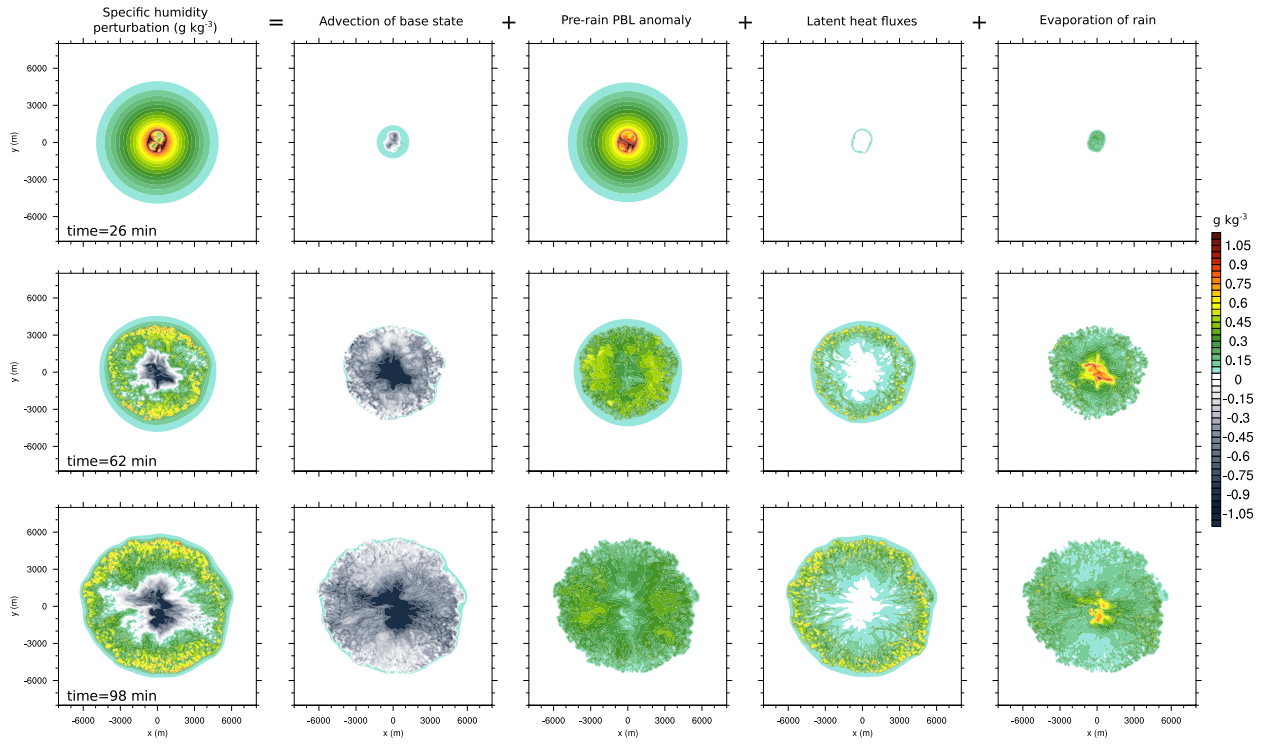


Figure 1. Decomposition of the (1st column) perturbation water-vapor mass fraction q'_v into contributions from (2nd column) the advection of the base-state perturbation q'_{base} , (3rd column) the advection of the pre-rain PBL anomaly q'_{pbl} , (4th column) latent-heat fluxes q'_{lh} , and (5th column) evaporation of rain q'_{er} . Distributions are from simulation R1 and shown after 26, 62, and 98 min. All quantities are computed as density-weighted vapor-mass fractions for the lowest 100 meters (see Eq. (6)). To obtain the perturbations in column 1 and 2, the far-field value of the base-state vapor mass fraction has been subtracted from the actual vapor mass fraction (1st column) and from the base-state mass fraction (2nd column). To very good approximation, the sum of the four rightmost panels yields the leftmost panel.

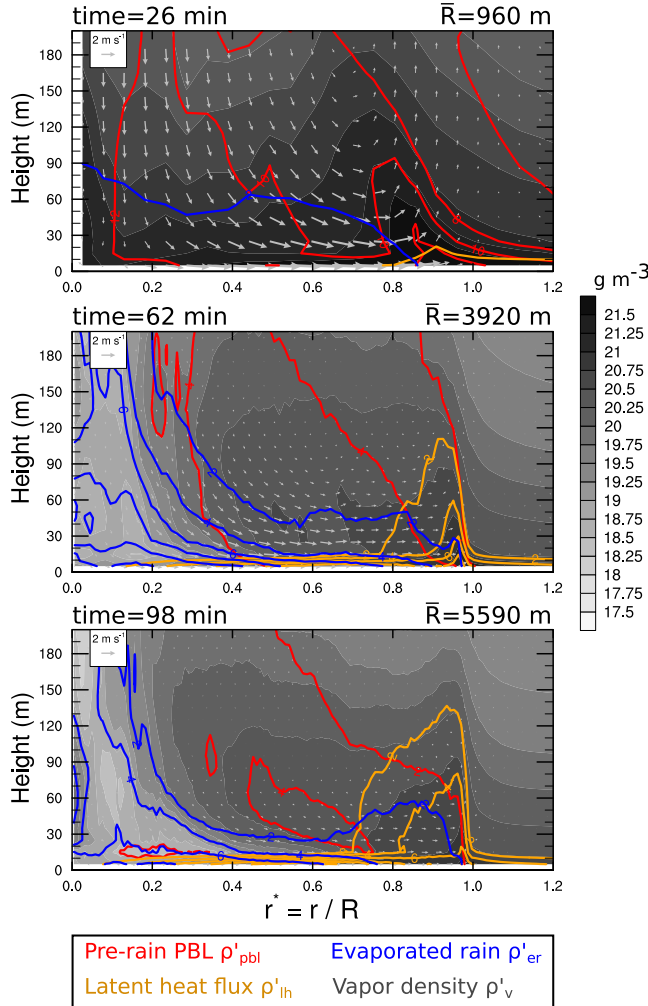


Figure 2. Azimuthally averaged r^* -z distributions of the water-vapor density ρ_v (g m^{-3} ; gray shading) and of the individual perturbations due to latent-heat fluxes ρ'_{lh} (orange contours), due to evaporation of rain ρ'_{er} (blue contours), and due to the pre-rain PBL anomaly ρ'_{pbl} (red contours) are shown for simulation R1 after 26, 62, and 98 min. The three perturbations are contoured every 0.2 g m^{-3} starting at 0.2 g m^{-3} (line labels are multiplied by 10). Vectors illustrate the average velocity field. A normalized radial distance $r^* = r/R$ has been computed first for each grid column with R the radius at the leading edge of the cold pool determined as described in the text. Averaging is then performed over r^* bins of width $dr^* = 50\text{m}/\bar{R}$ with \bar{R} the average R , which is indicated on top of each panel.

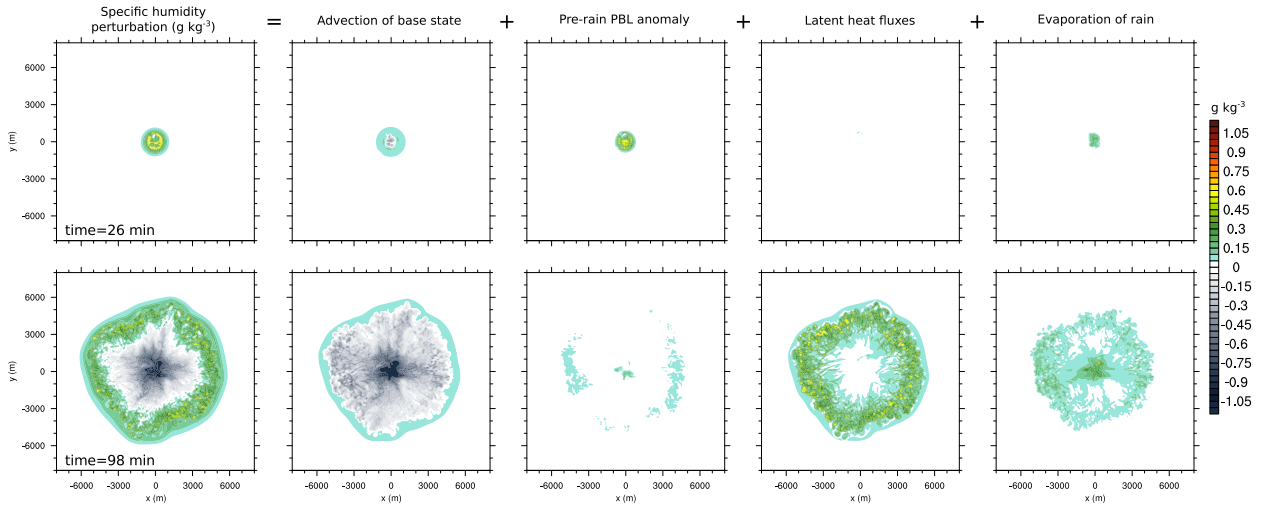


Figure 3. Same as Fig. 1, but for simulation R2, which is initialized without a moisture perturbation. Only two time steps are shown. The pre-rain PBL water-vapor perturbation visible here is only caused by surface latent-heat fluxes during the period of convergent near-surface flow.

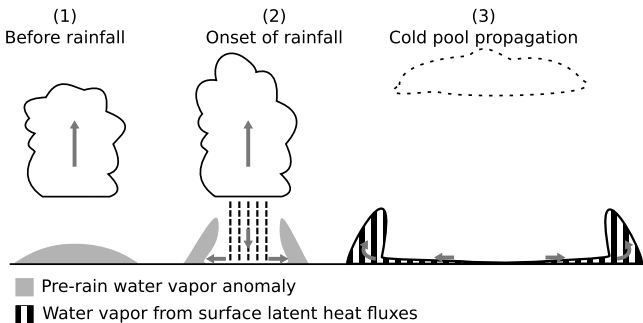


Figure 4. Schematic of the processes responsible for water-vapor rings in tropical cold pools.

(1) A water-vapor perturbation exists below cloud base before rainfall sets in. Deep convective clouds rise from sub-cloud layers that are relatively moist due to, e.g., the vapor ring of an older cold pool. Even without a pre-existing vapor ring, the pre-rain moisture excess below cloud base can result solely from enhanced surface fluxes during the early convergent period of cumulus growth. (2) The weight of rain drops is sufficient to maintain a downdraft that displaces the sub-cloud layer out of the rain shaft such that the exposure time of the sub-cloud layer to rain evaporation is short. The displaced and undercut air mass is relatively moist primarily due to the pre-rain water-vapor anomaly; the source from rain evaporation remains secondary. (3) The cold cool spreads radially and surface latent-heat fluxes continuously supply water-vapor mass that gets fluxed towards and into the leading edge of the cold pool.